CO Electroreduction on Single-Atom Copper

Yuxuan Wang[1, †], Boyang Li[2, †], Bin Xue[1,3, †], Nicole Libretto[4, †], Zhenhua Xie[5], Hao Shen[1], Canhui Wang[1], David Raciti[6], Nebojsa Marinkovic[5], Han Zong[1], Wenjun Xie[1], Ziyuan Li[1], Guangye Zhou[1], Jeff Vetik[1], Jingguang G. Chen[5], Jeffery Miller[4], Guofeng Wang[3, *], Chao Wang[1, *]

[1] Department of Chemical and Biomolecular Engineering, Johns Hopkins University, Baltimore, Maryland 21218, United States

[2] Department of Mechanical Engineering and Materials Science, University of Pittsburgh, Pittsburgh, Pennsylvania 15261, United States

[3] Department of Chemistry, College of Food Science and Technology, Shanghai Ocean University, Shanghai 201306, China

[4] Davidson School of Chemical Engineering, Purdue University, West Lafayette, Indiana 47907, United States

[5] Department of Chemical Engineering, Columbia University, New York City, New York 10027, United States

[6] Materials Science and Engineering Division, National Institute of Standards and Technology, Gaithersburg, Maryland 20899, United States

[†]These authors contributed equally to the work.

[*]Email: chaowang@jhu.edu; guw8@pitt.edu

Abstract

Electroreduction of CO_2 or CO toward value-added C_{2+} hydrocarbons represents a promising approach toward carbon-negative electrosynthesis of chemicals. Fundamental understanding of the C-C coupling mechanisms in such electrocatalytic processes is the key to the design and development of electrochemical systems at high energy and carbon conversion efficiencies. Here we report the investigation of C-C coupling mechanisms on single-atom Cu electrocatalysts. Atomically dispersed Cu was coordinated on a carbon nitride (C_3N_4) substrate to form high-density Cu-N_2 moieties. Surface-specific chemisorption, electrocatalytic and computational studies are combined to probe the C-C coupling kinetics. Unlike the Langmuir-Hinshelwood (L-H) mechanism known for metallic Cu catalysts, the confinement of CO adsorption on the single-metal-atom active sites enables an Eley-Rideal (E-R) type of C-C coupling between *CO and CO(g). The isolated copper sites also selectively stabilize the key reaction intermediates determining the bifurcation of reaction pathways toward different C_{2+} products.

One Sentence Summary

C-C coupling mechanisms on single-atom Cu electrocatalysts enables CO reduction to value-added hydrocarbons.

INTROUDCTION

Renewable energy-driven electroreduction of CO_2 represents a promising approach toward artificial carbon recycling.(*1, 2*) Electrolytes of high alkalinity are known to favor C-C coupling, a key step toward value-added C_{2+} hydrocarbon products such as ethylene, ethanol, acetate and *n*-propanol.(*3, 4*) However, CO_2 dissolves in aqueous electrolytes to form carbonic acid (H_2CO_3), which reacts with hydroxide and causes degradation of the electrolyte.(*5*) This challenge can be circumvented by sequential electroreduction of CO_2 to CO and then CO to C_{2+}.(*6-12*) Conversion of CO_2 to CO can be carried out in a bicarbonate buffer (e.g., $KHCO_3$), for which >90 % Faradaic efficiency (FE) toward CO has been demonstrated using noble metals such as Au(*13-15*) and Ag(*16*) or single-metal-atom(*17, 18*) electrocatalysts. Meanwhile, the electroreduction of CO can be done using high-alkalinity electrolytes to take advantage of the enhanced C_{2+} selectivities.(*10, 19-24*)

Metallic copper has been the sole monometallic catalyst known for favoring C_{2+} products in CO_2 and CO electroreduction with significant activity.(*6, 25, 26*) The rate of C_{2+} production is typically limited by the C-C coupling step between adjacent *CO(H) adsorbates, which is sensitive to the surface structure of Cu.(*19, 20, 26*) On Cu(100) and (110), the surface atoms with a four-fold symmetry are able to accommodate and stabilize the transition state of C-C coupling between two bridge-adsorbed *CO.(*8, 27-31*) Such *CO-*CO dimerization is mediated by electron transfer and has a lower energy barrier than C-C coupling after a hydrogenation step, e.g., between *CO and *CHO (or *COH). The latter likely takes place at relatively high overpotentials on Cu(111),(*32, 33*) although *CO-*CO dimerization has also been cited to account for the selective reduction of CO to acetate on this type of metal surface.(*31, 34*) Nevertheless, the understanding of CO_2/CO reduction pathways toward C_{2+} products thus far is largely limited to the Langmuir-Hinshelwood (L-H) mechanism, which usually requires high coverages of adsorbing intermediates.(*35*) While Cu binds to *CO(H) relatively weakly, other transition metals such as Pt and Pd bind CO too strongly and suffer from CO poisoning.(*36*) Advanced electrocatalytic materials with

alternative C-C coupling mechanisms and enhanced selectivity ward a specific C_{2+} product remains imperative for the further development of CO_2/CO reduction electrocatalysis.

Here we report a single-atom Cu electrocatalyst for selective reduction of CO to acetate (**Figure 1**). By co-pyrolysis of copper chloride ($CuCl_2$) and urea (see the Methods for details), atomically dispersed Cu is supported on carbon nitride (denoted as Cu_1@n-C_3N_4) and stabilized via copper-nitrogen coordination (**Figure 2A**). The Cu_1@*n*-C_3N_4 electrocatalyst exhibits high activity for selective reduction of CO to multi-carbon products, with the overall FE toward C_{2+} (FE_{C2+}) reaching 74 %. In particular, acetate is the dominant product with $FE_{acetate}$ achieving ~50 %, which surpasses many known electrocatalysts for acetate production under similar conditions (**Table S1**). A combination of kinetic and isotopic studies reveals that a unique Eley-Rideal (E-R) mechanism accounts for C-C coupling on the isolated copper sites. This mechanism was further corroborated by performing density functional theory (DFT) calculations, which illustrates the distinct adsorption configurations of key reaction intermediates that determine the C-C coupling mechanisms and the following bifurcation of reaction pathways toward different C_{2+} products.

RESULTS

Synthesis and characterization of Cu single-atom-electrocatalysts (SAECs). Two Cu SAECs were prepared with 27 wt% and 10 wt% of metal loading (denoted as Cu_1@n-C_3N_4−27% and Cu_1@n-C_3N_4−10%), for which the element compositions were characterized by using electron energy loss spectroscopy (EELS) and inductively coupled plasma atomic emission spectroscopy (ICP-AES) (**Figure S1**). Pristine C_3N_4 derived from the pyrolysis of urea in the absence of $CuCl_2$ was used as a control.(*37*) The high metal loading in Cu_1@C_3N_4−27% is in line with the theoretical capacity (26.3 wt%) of graphitic carbon nitride (*g*-C_3N_4) if one Cu atom is presumably anchored on each unit cell (**Figure S2**), albeit that the C:N atomic ratios are off the stoichiometry of C_3N_4 (56:44 and 47:52 for Cu_1@*n*-C_3N_4−10 % and Cu_1@*n*-C_3N_4−27 %, respectively). X-ray diffraction (XRD) patterns of these materials show typical peaks of C_3N_4 and no

features are found to be associated with copper metal or copper oxides (**Figure S3**). The strongest peak at 27.5° can be assigned to the (002) lattice plane of g-C_3N_4, corresponding to a *d*-spacing of 0.323 nm between the stacked graphitic layers of C_3N_4. The absence of aggregated copper species is confirmed by both low- and high-resolution transmission electron microscopy (TEM) imaging (**Figures S4 and S5)**. High-angle annual dark-field scanning transmission electron microscopy (HAADF-STEM) images show that the majority of Cu species is dispersed as individual atoms. The bright-field STEM image shows a layered structure with an inter-layer *d*-spacing of ~0.33 nm, consistent with the distance of (002) lattice plane derived from XRD analysis (**Figure S6**).

Elemental composition mapping based on electron energy loss spectroscopy (EELS) shows uniformly distributed Cu species at high densities on the C_3N_4 substrate (**Figure 2B**). Line-profile analysis suggests that the distribution of Cu is more tightly correlated to N than C, indicating the preferential anchoring of Cu at the nitrogen sites on the substrate (**Figure S7**). The EELS spectra for Cu_1@n-C_3N_4 exhibit white-line features with onsets at ~933 eV and ~953 eV. Compared to the various references including Cu, Cu_2O and CuO, these features can be assigned to the L_3 and L_2 absorption edges of Cu^{1+}, suggesting an oxidation state of +1 for the copper species in the SAECs (**Figure 2C**). This finding is corroborated by X-ray photoelectron spectroscopy (XPS) measurements (**Figure S8**), as evidenced from the absence of characteristic Cu^{2+} satellite peak in Cu 2p XPS spectrum and the 916.8 eV ($L_2M_{45}M_{45}$) peak in Cu Auger LLM spectrum. The N 1s XPS spectra was fitted to compare the coordination environments between C_3N_4 and Cu_1@n-C_3N_4-27% (**Figure S9**). Notably, Cu_1@n-C_3N_4-27% exhibits a much more pronounced feature associated with the tri-coordinated N (M-N-C_2) than for C_3N_4, consistent with the expectation for Cu-N coordination.(*38*)

Atomic structure of the Cu SAECs was resolved by performing X-ray absorption spectroscopy (XAS) measurements. X-ray absorption near edge structure (XANES) regions of both Cu_1@n-C_3N_4−27 % and Cu_1@n-C_3N_4−10 % exhibit onsets at 8.982 keV, which resembles the case for Cu_2O but distinguishes from Cu (8.981 keV) and CuO (8.985 keV) (**Figure 2D**).(*39, 40*) The XANES spectra of Cu_1@n-C_3N_4 are

also distinct from Cu(II) tetraphenylporphyrin (Cu-TPP), an organometallic compound with four-fold Cu-N coordination (**Figure S10**), by showing no pre-edge feature around 8.978 keV, with the latter being characteristic of Cu^{2+} (**Figure 2E**).(*41*) The XANES analysis is thus consistent with EELS and confirms the 1+ oxidation state of Cu in the SAECs. The local atomic coordination around the Cu centers was inferred by fitting the extended X-ray adsorption fine structure (EXAFS) spectra (**Figure 2F**). The first-shell fit demonstrates that Cu_1@n-C_3N_4−27% and Cu_1@n-C_3N_4−10% contains 1.8 and 1.7 Cu-N bonds, respectively, with a bond length of 1.91 Å (**Table S2;** see the details of fitting in **Figure S12**). This short bonding distance is in line with the Cu-N bonding distance observed in Cu-TPP (1.98 Å), whereas typical Cu-O bond distances in reference oxides (CuO and Cu_2O) exceed 2.00 Å. No Cu-Cu bond was observed, confirming the single-atom dispersion of Cu in the SAECs.

Electrocatalytic Studies for CO Reduction. The electroreduction of CO was measured by using a gas-diffusion electrode (GDE) cell and 1 mol/L KOH as the flowing electrolyte (**Figure S13A, B**).(*42, 43*) The products derived from Cu_1@n-C_3N_4−27% are mainly composed of C_{2+} hydrocarbons throughout the investigated potential range (from −0.5 to −1.0 V), which are dominated by acetate but still contain a trace amount of methane at potentials more negative than −0.6 V (**Figures 3A and S13C**). FE_{CH3COO^-} reaches 46 % at −0.5 V and persists at more negative potentials, with the maximum, 48%, recorded at -0.8 V (**Figure 3B**). Ethylene also appears at −0.5 V, with a relatively low FE (FE_{CH2CH2}) of 3 %. Ethanol and *n*-propanol are present in the products obtained at potentials more negative than −0.7 V, with corresponding FE_{C2H5OH} and FE_{C3H7OH} found to be at ~8% and ~6 %, respectively. The FE toward methane (FE_{CH4}) is merely 4 % at most as observed at −1.0 V. Noticeably, the high activity and selectivity of Cu_1@n-C_3N_4−27% persists through elongated operations. In a chronopotentiometric stability test at 60 mA/cm^2, the overpotential was quite stable throughout a period of 24 hours and FE_{CH3COO^-} only changed slightly from 48% at the beginning to 44 % at the end (**Figure 3C**). Compared to the previously reported electrocatalytic performances of Cu nanocrystals for CO reduction, the Cu SAECs behave more like Cu(111) nanosheets in terms of selective production of acetate, as compared to Cu nanocubes (with (100) dominated surface)

that favors ethylene production.(*34*) However, the discrete, namely absence of continual copper-atom ensembles, and cationic (+1, vs. metallic Cu^0) nature of the active sites suggest a different catalytic mechanism toward the same C_2 product, acetate, on the Cu SAECs.

We have further compared C_3N_4 (**Figure S14**) and Cu_1@n-C_3N_4-10% (**Figure S15**) with Cu_1@n-C_3N_4-27% for CO reduction. At −1.0 V, Cu_1@n-C_3N_4−27% delivers the highest total current density per geometric area of the electrode (J_{tot}), which achieves 104 mA/cm^2(versus reversible hydrogen electrode, RHE; the same potential scale is used in the following discussion unless otherwise specified) (**Figure 3D**). At this potential, Cu_1@n-C_3N_4-10% and C_3N_4 deliver 63 and 14 mA/cm^2, respectively. Similar trend exhibits in the current density of CO reduction (J_{CO}), which reads at 83.9 and 28.1 mA/cm^2 at −1.0 V for Cu_1@n-C_3N_4-27% and Cu_1@n-C_3N_4-10%, respectively (**Figure 3E**). No CO reduction product in significant amount but H_2 was obtained from the control experiment with g-C_3N_4 (**Figure S14**). Moreover, the selectivity also correlates tightly to the Cu loading. For example, FE_{CH3COO^-} reads at 0 %, 14 % and 48 % at −0.8 V for the three catalysts, corresponding to J_{CH3COO^-} of 0 mA/cm^2, 7.1 mA/cm^2 and 32.9 mA/cm^2, respectively (**Figure 3F**; also see **Figures S14-15** for more electrocatalytic results of Cu_1@n-C_3N_4-10% and C_3N_4). The consistent trend of Cu_1@n-C_3N_4-27 % > Cu_1@n-C_3N_4-10 % > C_3N_4 for both current density and FE indicates that the atomically dispersed Cu is not only the active site for activation of CO, but also accounts for C-C coupling and restriction of the consequent reaction pathways toward specific C_2 products. This is congruent with the control experiment performed on Cu nanoparticles supported on C_3N_4, which does not show comparable performance with the Cu SAECs for electroreduction of CO to acetate (**Figure S16**). Moreover, electrocatalytic studies using isotope labeled ^{13}CO confirmed that both carbon atoms in the acetate product were derived from the reduction of carbon monoxide (**Figures S17-S18**).

Active Sites and Kinetic Studies. The assignment of single-atom Cu as the active site is corroborated by performing diffuse reflectance infrared Fourier transform spectroscopy (DRIFTS) and CO stripping voltammetry analyses. In the DRIFTS spectra collected on Cu_1@n-C_3N_4-27 % and Cu_1@n-C_3N_4-10 % with CO preabsorbed at room temperature, a peak appears at 2,098 cm^{-1}, which is absent in the case

of C_3N_4 (**Figure 4A**). This feature can be assigned to the stretching of C=O bond in linearly absorbed *CO.(*18, 44, 45*) In line with the observations from DRIFTS, the CO stripping voltammetry (recorded at room temperature in 0.1 mol/L of KOH, see the experimental details in the Methods) recorded on Cu_1@n-C_3N_4-27 % and Cu_1@n-C_3N_4-10 % exhibit a peak at 0.28 V, which is not seen for C_3N_4 (**Figure 4B**). The peak intensities integrated from the CO stripping voltammetry increases with metal loading (**Figure S19**), signaling that the observed *CO features are indeed associated with the uniformly distributed single-atom Cu sites. Noticeably, the previous studies of temperature programmed CO desorption (CO-TPD) show that *CO desorbs from metallic Cu surfaces below or at room temperature.(*31, 46*) Meanwhile, no such features were observed in our control experiments on the C_3N_4 supported Cu nanoparticles (**Figure S20**). Thus atomically dispersed Cu sites in the SAECs are believed to possess distinct adsorption properties from their metallic counterparts, and thereby give rise to dissimilar catalytic mechanisms for CO reduction. As to be shown below by computational simulations, such a difference is corroborated by the much stronger binding of CO on the single-atom Cu sites than on continuous Cu surfaces.

The durability of the Cu SAECs was revealed by in-situ XAS studies, which showed nearly no change in either XANES or EXAFS spectra under reaction conditions (**Figures 4C, D and S21**). The structural fitting parameters derived from the in-situ EXAFS spectra are included in **Table S2**. We found that the coordination number of Cu in Cu_1@n-C_3N_4 increased from 1.7~1.8 (measured ex-situ, protected with Kapton tape and kept from exposure to air) to 2.7~2.8 under the CO reduction reaction condition. Such a difference can be attributed to the adsorption of CO, as the Cu-N (1.91 Å) and Cu-C (1.78 Å for Cu-*CO) bonding involved in the Cu_1@n-C_3N_4 electrocatalysts are nearly indiscernible in EXAFS. Due to the strong Cu-*CO binding (as predicted from the DFT calculations and confirmed with the chemisorption analysis using FTIR), the coverage of *CO on the single-atom Cu sites is expected to be high (near one monolayer) during the reaction. Such adsorbate induced changes in coordination number have also been observed in the previous in-situ XAS studies of transition metals (such as Pt and Pd) that binds strongly to CO.(*47, 48*)

Given with the clear indication of single-atom Cu being the active sites, we then turn our effort to find out the rate-limiting step (RDS) of CO reduction on such sites. For that purpose, we performed kinetic analysis of the reaction order with respect to CO and the Tafel slope in terms of J_{CH3COO^-}. In the former case, the electroreduction of CO was measured at various CO partial pressures (P_{CO}). While the total current densities remain quite consistent, J_{H2} decreases from 11.5 mA/cm^2 at P_{CO} = 0 to 4.6 mA/cm^2 at P_{CO} = 1 atm, corresponding to increase of CO reduction current density from 0 to 10.1 mA/cm^2 (**Figure 4D**). Product distribution shares a similar trend, namely decreasing FE_{H2} and increasing FE_{C2} with P_{CO} (**Figure 4E**). We have further analyzed the reaction order (*n*) with respect to CO for the reduction of CO to acetate, the major C_2 product. *n* is found to exhibit divergent values at different P_{CO} (**Figure 4F**). In the low-P_{CO} region (0~0.15 atm), the rate of acetate production is nearly first order with respect to CO. The reaction seems to approach saturation at P_{CO} > 0.3 atm and the rate of acetate production becomes weakly dependent on the CO concentration, where *n* drops to 0.15. Between these two extremes is obviously a transitional region with an intermediate *n* of 0.49. In line with the observations in terms of reaction orders, the slope (η) derived from the Tafel plot for J_{CH3COO^-} also diverges at high- and low-P_{CO}, determined to be −123 and −406 mV·dec^{-1} at P_{CO} = 1 and 0.15 atm, respectively (**Figure 4G**).

Comparing these kinetic parameters to those expected for the different RDSs of C_{2+} product formation(*49, 50*) (**Table S3**), the high-P_{CO} case with nearly zero reaction order and a Tafel slope of −123 mV·dec^{-1} for acetate production indicates that the reaction rate is limited by the hydrogenation of *CO to *CHO (or *COH), via

$$^*CO + H_2O + e^- \xrightarrow{k_1} {}^*CHO + OH^- \quad (1)$$

Hereby it should be noticed that the hydrogen is sourced from water molecules instead of co-adsorbed *H, as otherwise one would expect a negative CO reaction order and a lower Tafel slope.(*21*) Owing to the strong binding of *CO (calculated to be 0.94 eV, see the discussion below for computational simulations), the coverage of intermediate adsorbates (*CO, *CHO, etc.) on the single-atom Cu sites is likely not (or weakly) dependent on P_{CO}, giving rise to a nearly zero order with respect to CO. At low P_{CO}, the scenery

with first-order and a Tafel slope of −406 mV·dec^{-1} in combination for acetate production is unprecedented for any known RDS of CO reduction toward C_{2+} (**Table S3**), indicating a distinct reaction pathway on the Cu SAECs as compared to the extensively studied metallic Cu electrocatalysts. After detailed analysis (see the Supporting Information for the details of kinetic modeling), we ascribe it to an Eley-Rideal mechanism on the single-atom Cu sites

$$^{*}CHO + CO(g) \xrightarrow{k_2} {}^{*}CHOCO \quad (2)$$

This RDS is a non-Faradaic process and depends weakly on the electrode potential, giving rise to the largely negative Tafel slope. Similar to the argument at high P_{CO}, the coverage of *CO on the single-atom Cu sites is likely high under the reaction conditions, which can be assumed to be independent of the CO partial pressure even at relatively low P_{CO}. Thereby the RDS (2) is first order with respect to CO.

It should be pointed out that the above two sceneries are not necessarily mutually exclusive and the two steps (1) and (2) can take place sequentially in a consistent reaction pathway toward C_{2+} products (**Figure 4I**). The shift of RDS from (1) to (2) at reduced P_{CO} can simply be due to the slower rate of the Eley-Rideal step at low P_{CO}, whereas the CO hydrogenation step remains unchanged. As discussed above, such a difference can be ascribed to the strong binding of *CO and saturated coverage of *CO/*CHO on the single-atom Cu sites. We also notice that the Eley-Rideal mechanism described in RDS (2) differs from the previously reported C-C coupling mechanism between *CO and CO(g)(*51*) via

$$^{*}CO + CO(g) \xrightarrow{k_3} {}^{*}C_2O_2 \quad (3)$$

Reaction (3) has been proposed as a possible pathway toward ethylene production on metallic Cu surfaces at high P_{CO}, in addition to the C-C coupling between two adjacent *CO.(*19, 20, 51, 52*) This pathway would not give the high-P_{CO} performance as seen for the Cu SAECs here, although it cannot be excluded for the low-P_{CO} case. As to be elucidated below, our computational simulations have shown that the formation of $*C_2O_2$ on the single-atom Cu sites is highly unfavorable, and thereby the pathway via (3) is not considered. On the other side, even though a span of SAECs has been reported to produce C_{2+} products such as

ethylene(*53, 54*) and ethanol(*55*), but the possible involvement of E-R mechanism for C-C coupling was not explicitly discussed in those studies. The advantage of the E-R mechanism in Cu_1@n-C_3N_4-27% is its selectivity for a specific C_{2+} product, reaching >50% FE toward acetate. This performance is superior to many Cu-based electrocatalysts relying on the L-H mechanism (e.g., a multi-hole cuprous oxide catalyst had only 35% FE towards ethylene as its most selective product, albeit with higher overall FE for C_{2+}(*56*)).

Computational Simulations. To corroborate the reaction pathway derived from the above kinetic analysis, we have performed density functional theory (DFT) calculations to simulate the CO reduction pathways on single-atom Cu sites. Among the various Cu-N_x configurations (x = 2, 3, 6; **Figure S22**) that are possible for anchoring Cu on the g-C_3N_4 substrate, Cu-N_2 with one copper atom coordinated to each unit cell of g-C_3N_4 via two Cu-N bonds (**Figure S23**), at a 75° bonding angle, is predicted to be the energetically most favorable (**Figure S24**, **Table S4**). Noticeably, the formation of four-fold metal-nitrogen coordination (Cu-N_4), which is more commonly seen for single metal atoms anchored on nitrogen-doped carbon substrates (M-N-C),(*18, 57-59*) is found to be energetically unfavorable on g-C_3N_4, as envisioned from its incompatibility with the three-fold symmetry of the g-C_3N_4 lattice. Our calculations further reveal that the oxidation state of Cu in the Cu-N_2 center is +1 (**Figure S25-26** and **Table S5**). Also, the dimeric configuration of copper center on the g-C_3N_4 substrate (Cu_2@n-C_3N_4, **Figure S27**) was found to be energetically less favorable than the monomers by ca. 0.99 eV. These results are consistent with the experimental characterizations for the Cu_1@n-C_3N_4 catalysts, *i.e.*, Cu(I) is anchored on the C_3N_4 substrate with a Cu-N coordination number of ca. 2 and no Cu-Cu bonding is present (**Figure 2F and Table S2**). In addition, simulation of possible demetallation processes due to reduction of Cu(I)(*59, 60*) indicates that the Cu-N_2 center is stable at potentials as negative as −1.0 V vs. RHE (**Figure S28 and Table S6**), resembling the high stability of Cu_1@n-C_3N_4 derived from in-situ XAS characterizations (**Figure 4C, H**).

CO is found to bind strongly on the Cu-N_2 site with an adsorption energy of −0.94 eV (**Table S7**). In comparison, the values on Cu(100) and Cu(111) are −0.53 eV and −0.47 eV, respectively. The much stronger binding of CO on the single-atom Cu sites compared to the metallic copper surfaces is in line with

the C=O vibrational feature observed from DRIFTS in the former case but not for the control with Cu nanoparticles (**Figures 4A and S29**). It is noted that, in the Cu_1@n-C_3N_4 catalyst, adsorption of CO on the N and C sites adjacent to Cu is not favorable (e.g., 0.24 eV for *CO on C, while *CO on the N site will transfer to the neighboring C site spontaneously; **Table S8**), and thereby Cu is likely the only active site accommodating CO adsorption in the SAECs. This finding is also consistent with the observations of single *CO features on the Cu_1@n-C_3N_4 catalyst using DRIFTS (**Figure 4A**) and CO stripping (**Figure 4B**), but not for the C_3N_4 substrate. The resolved adsorption properties of Cu_1@n-C_3N_4 thus confirm the atomically dispersed Cu as the active site for CO reduction.

With Cu identified as the active sites, we predict that the electroreduction of CO on Cu_1@n-C_3N_4 starts from CO adsorption and protonation to form *CHO (reaction (1)) (**Figures 5, S31-34**). Subsequently, C-C coupling via an E-R mechanism (reaction (2)) takes place between the *CHO adsorbing on Cu and another gas-phase CO molecule (or dissolved in the electrolyte) to form a *CO-CHO. This C_2 intermediate is further hydrogenated to form *CO-CHOH, *CHCO and *CH_2CO, sequentially. Eventually, *CH_2CO could react with a water molecule to produce acetic acid, or with an OH^- to form acetate (**Figures 5A and B**). The *CHO-CO(g) coupling step has a kinetic barrier of 0.80 eV (See Supplementary **Figure S31A**), which is comparable to that for the C-C coupling via the Langmuir-Hinshelwood mechanism (*CO + *CO → *OCCO) on Cu surfaces.(*20, 59*) This value is also lower than that (0.83 eV with water as the hydrogen source,(*21*) **Figure S35**) for the hydrogenation of *CO to *CHO on the single-atom Cu sites. The latter, *i.e.*, reaction (1), involves proton coupled electron transfer and turns out to be the rate-determining step (RDS) for the overall free-energy reaction coordinate to acetate, which agrees with the finding derived from kinetic analysis for high-P_{CO} conditions. The transition of RDS from CO hydrogenation at high P_{CO} to C-C coupling at low P_{CO} can be understood via the increase of free energy barrier at reduced CO partial pressure (**Figure S32**). The alternative *CO + CO(g) coupling path (reaction (3)), in which the C-C coupling occurs before the protonation of CO, is predicted to have a free-energy barrier of 2.21 eV, much higher than those

for the *CHO + CO(g) coupling and the protonation of *CO and is thus considered to be unfavorable on the Cu SAECs (**Figure S34**).

The E-R mechanism described above is believed to be more favorable than possible L-H type of C-C coupling on the Cu_1@n-C_3N_4 catalyst. Co-adsorption of two C_1 species, such as *CO and/or *CHO, on a single Cu site is highly unstable with a positive adsorption energy of 0.25 eV (**Table S9**). The activation energy for C-C coupling via the L-H mechanism (*CO + *CHO → *COCHO) is calculated to be 2.45 eV, unsurmountable at room temperature, suggesting that the C-C coupling unlikely goes through the L-H mechanism on the Cu_1@C_3N_4 electrocatalysts (**Figure S31B**). This is distinct from the case on metallic Cu surfaces, where the continual surface is essential for accommodation of the L-H type of C-C coupling mechanism between neighboring adsorbates.(*20, 61*) We note that the free energies of *CHO adsorbing on the Cu site and its adjacent C site are quite similar, which are calculated to be −0.09 eV and 0.00 eV, respectively (**Table S9**), invoking the possible migration of *CHO from the former to the latter.(*62*) However, the smallest distance between the *CHO adsorbing on C and the *CO on Cu is found to be about 3.8 Å, quite larger than any value known for C-C coupling (e.g., ~3.3 Å for *CO-*CO coupling on Cu(100), see **Figure S30** for the details of modeling). In addition to this concern, the reaction order with respect to CO is expected to be nearly zero at low P_{CO} for the pathway with C-C coupling between *CO on Cu and *CHO on C, considering the strong binding of *C(H)O on these sites. This would not be consistent with the first order derived from experimental measurements (**Figure 4F**). Thereby, the L-H type of C-C coupling mechanism can be excluded for the electroreduction of CO on the Cu SAECs.

After determining the C-C coupling mechanism, we further examined the bifurcation of reaction pathway toward different C_2 products. The continual reduction of *CHCO can form either *CH_2CO or *CHCHO (**Figures 5A, B**). It has previously been reported that, during the electroreduction of CO, *CH_2CO is the intermediate toward acetic acid, whereas *CHCHO mainly leads to ethylene or ethanol.(*19, 34*) On the Cu-N_2 site, the selectivity toward different C_2 products is determined by the free energy change of two competing reactions, *CH-CO → *CH_2CO toward acetate and *CH-CO → *CHCOH toward

ethylene and ethanol. After including the solvation effect in our calculations, we predict that the free energy change to be −0.15 eV for the *CH-CO → *CH_2CO step and 0.94 eV for *CH-CO → *CHCOH at U = 0 V (**Figure 5A**), with the former being more favorable by >1 eV than the latter but both are independent of P_{CO} on the strongly binding single-atom Cu sites. It should be noted that, while *CHCHO binds to the Cu-N_2 site via a single C-Cu bond, *CH_2CO coordinates onto the single-copper-atom site via two C-Cu bonds, forming a three-membered ring with Cu with a π bond (**Figure 5C**). Both the π bond and the four-fold coordination of Cu are believed to be crucial for the stabilization of *CH_2CO on the Cu-N_2 site. This is in contrast to the case on metallic copper surfaces, where *CH-CHO is thermodynamically much more stable on Cu(100) than *CH_2CO, causing more favorable formation of ethylene (**Table S10**).(*19*) In that case, the O atom in *CH-CHO could co-adsorb on the neighboring Cu site to form a five-membered ring, which is an energetically favorable structure (**Figure S30**). On the single-atom Cu without neighboring co-adsorption sites, *CH-CHO can only form an unstable tetratomic ring, which spontaneously transforms into the state with a single C-Cu bond (**Figure 5C**). Over the course of CO reduction on Cu_1@n-C_3N_4, higher P_{CO} makes the C-C coupling via the E-R mechanism *CHO + CO_g → *COCHO more favorable and thus gives rise to higher reactivity toward C_2 products, but the increase would mainly go toward acetate due to the dominance of *CH-CO → *CH_2CO over *CH-CO → *CHCOH toward ethylene. It thus explains the experimentally observed strong dependence of $J_{acetate}$ on the partial pressure of CO but not for $J_{ethylene}$ (**Figure 4G**).”

DISCUSSION

In summary, we have revealed a new C-C coupling mechanism for the electroreduction of CO single-atom Cu electrocatalyst, Cu_1@n-C_3N_4. This catalyst contains Cu(I)-N_2 active centers, on which E-R type of C-C coupling takes place between *CHO (formed via protonation of *CO strongly binding on Cu) and gas-phase CO. This E-R mechanism can explain the observed catalytic activity and selectivity, as well as

reaction kinetics in terms of reaction order with respect to CO and Tafel slope for acetate production. Moreover, we have also determined the relative stabilities of different C_2 intermediates post C-C coupling on the single-atom Cu site, which explains the selectivity toward C_2 hydrocarbons. Our work illustrates the great potential of single-atom electrocatalysts for the development of CO_2 and CO reduction electrocatalysts beyond Cu metal.

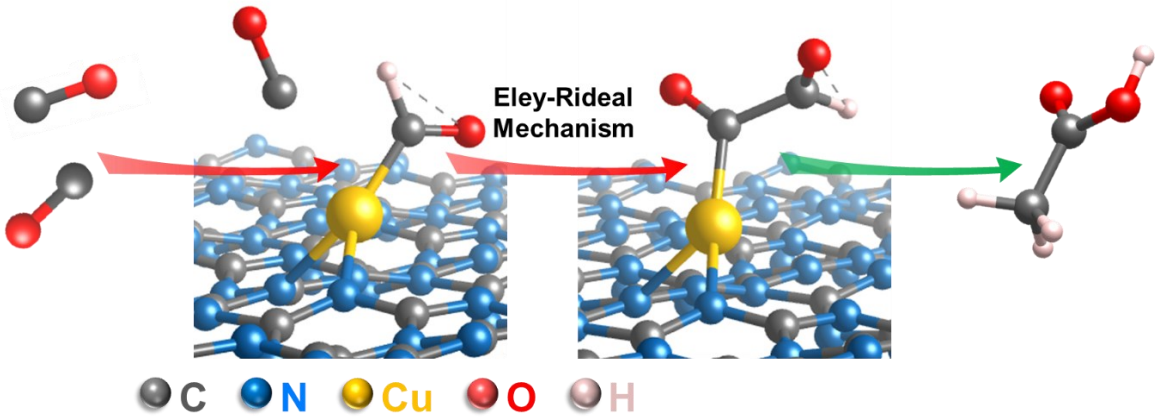

Figure 1. Scheme of Concept. Illustration of the Eley-Rideal (E-R) mechanism for CO electroreduction on Cu_1@n-C_3N_4.

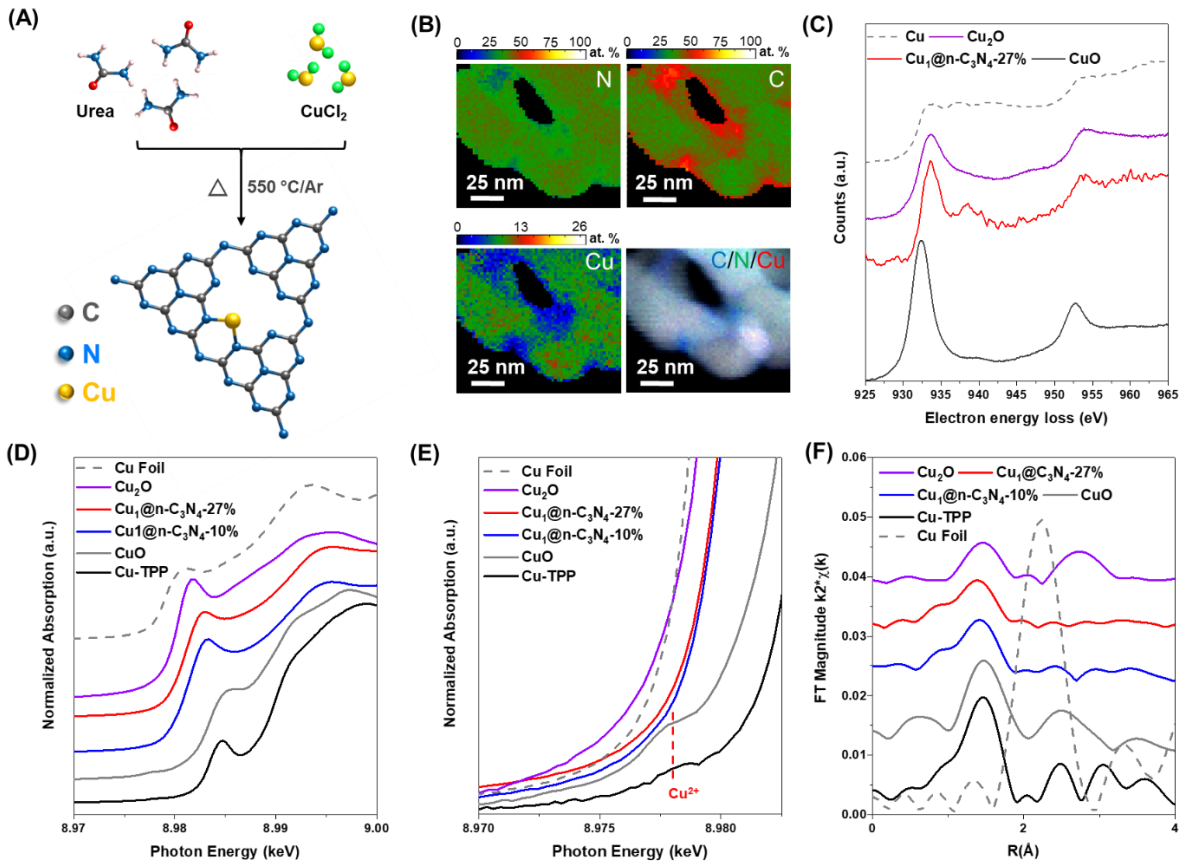

Figure 2. Synthesis and characterization. (A) Scheme for the synthesis of Cu_1@n-C_3N_4. (B) EELS-based elemental mapping (color contoured in at. %) on Cu_1@n-C_3N_4−27 %. (C) EELS spectra of Cu_1@n-C_3N_4−27 % and the references (Cu, Cu_2O and CuO). (D, E) EXANES and (F) EXAFS spectra of Cu_1@n-C_3N_4−27 %, Cu_1@n-C_3N_4−10 %, C_3N_4 and the references including Cu_2O, CuO, Cu-TPP and Cu foil.

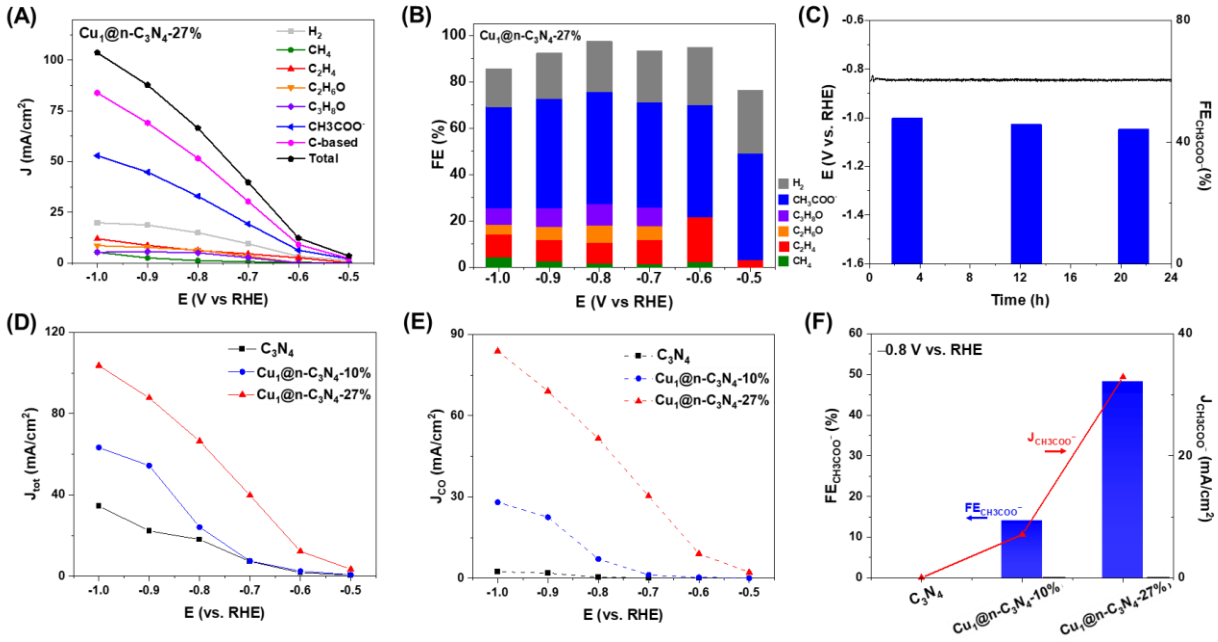

Figure 3. Electrocatalytic performance. (A) Partial current densities, (B) Faradaic efficiencies and (C) stability test of Cu_1@n-C_3N_4-27 %. Comparison of (D) total current density (J_{tot}), (E) partial current density for CO reduction (J_{CO}) and (F) Faradaic efficiency (FE_{CH3COO^-}) and current density (J_{CH3COO^-}) for acetate at −0.8 V among C_3N_4, Cu_1@n-C_3N_4-10 % and Cu_1@n-C_3N_4-27 %. I say that

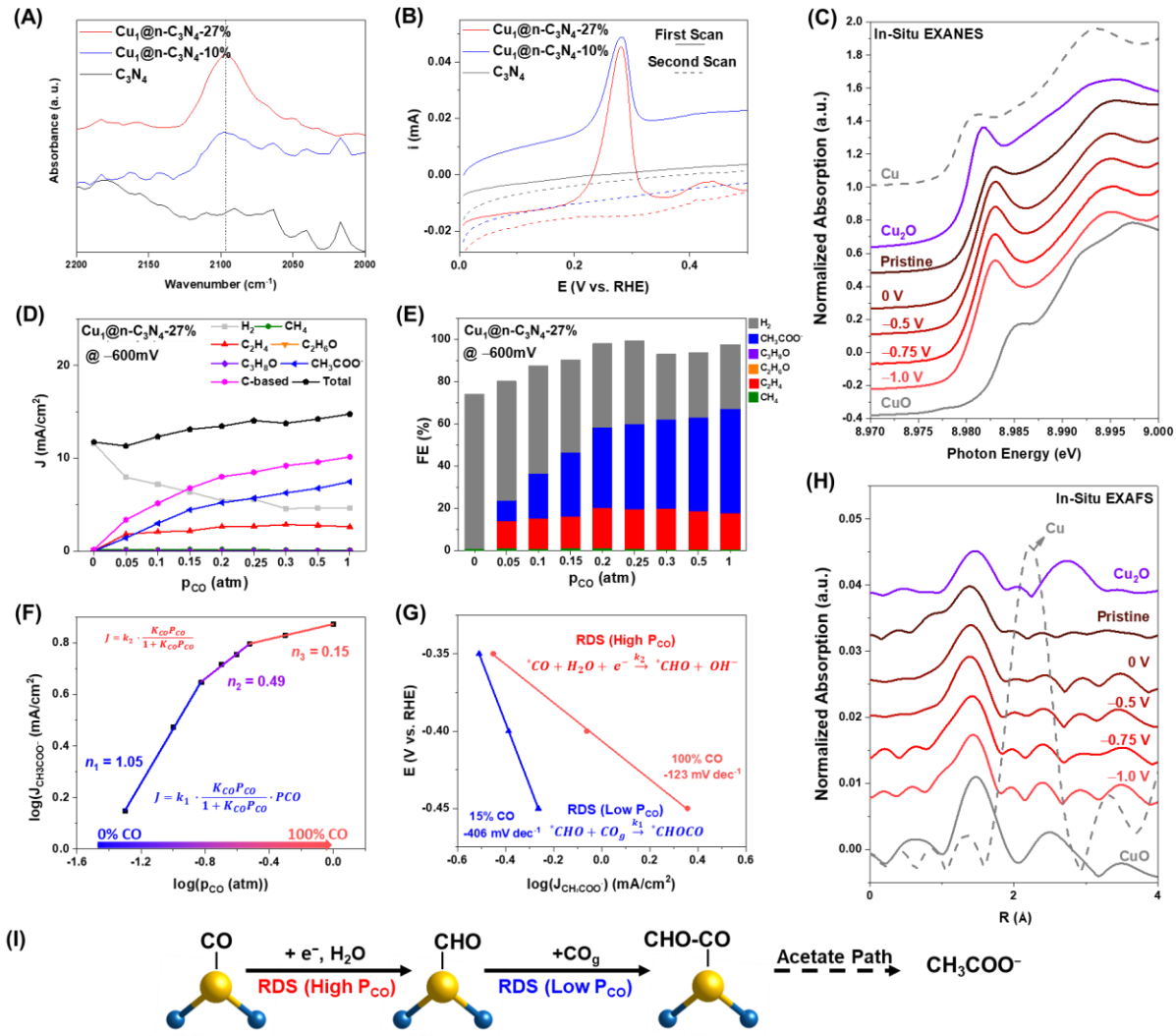

Figure 4. Active sites and kinetic studies. (A) DRIFTS spectra and (B) CO stripping voltammograms of Cu_1@n-C_3N_4-27%, Cu_1@n-C_3N_4-10 % and C_3N_4. (C) In-situ XANES and (D) Plot of partial current density for acetate versus CO partial pressure at −0.6 V. (E) Faradaic efficiencies of CO reduction products measured in dependence of P_{CO}, catalyzed by Cu_1@n-C_3N_4-27% at −0.6 V. (F) Kinetic plots showing the reaction order of acetate production with respect to CO. (G) Tafel plots at high- (1 atm) and low-P_{CO} (0.15 atm) conditions. (H) EXAFS spectra of Cu_1@n-C_3N_4-27% measured at 0 V, −0.5 V, −0.75 V and −1 V, with CO as the reactant gas and 1 mol/L KOH as the electrolyte. The spectra of Cu, Cu_2O, CuO and pristine Cu_1@n-C_3N_4-27% (recorded ex-situ) were overlapped for comparison. (I) Illustration of the two RDS sceneries associated with the E-R type of C-C coupling mechanism.

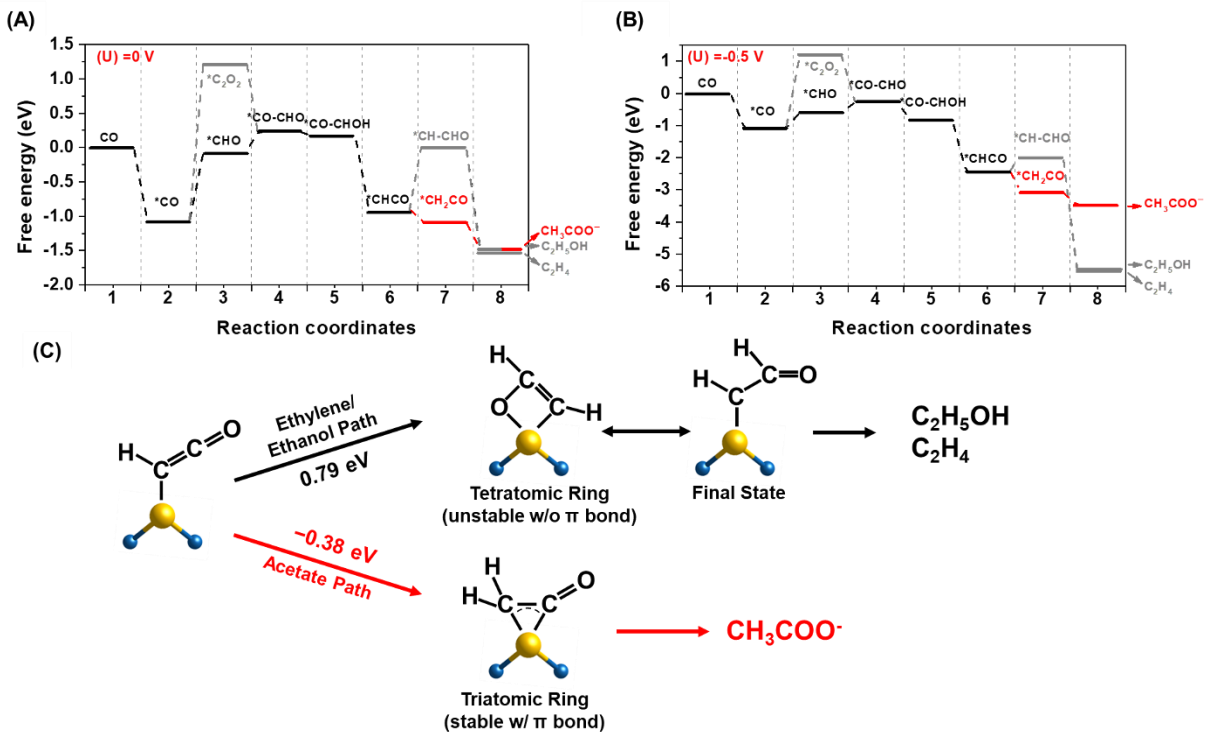

Figure 5. Computational simulations. Predicted free energy evolution for CO reduction to C_2 hydrocarbons on the Cu-N_2 site under an electrode potential of (A) 0 V/RHE, and (B) -0.5V/RHE. (C) Calculated free energy change for *CH-CO to *CH_2CO/*CH-CHO.

MATERIALS AND METHODS

Experimental Methods

Materials. Copper (II) chloride ($CuCl_2$, ⩾99.995%), urea (99.0-100.5%), potassium hydroxide (KOH, for CVs, 99.99%), Nafion™ 117 containing solution (~5% in a mixture of lower aliphatic alcohols and water) and carbon-^{13}C monoxide (^{13}CO, <5 atom % ^{18}O, 99 atom % ^{13}C) were purchased from Sigma Aldrich. Potassium hydroxide (KOH, for electrolysis, 85% min, K_2CO_3 2.0% max) was purchased from Alfa Aesar. Gas diffusion layer (GDL, Sigracet 39 BC) and anion exchange membrane (AEM, Fumasep FAB-PK-130) were purchased from Fuel Cell Store. All the materials were used without further purification. Electrolyte solutions were prepared using 18.2 MΩ H_2O (Elga Veolia).

Characterization. Transmission electron microscopy (TEM) images were acquired on a Phillips EM 420 microscope. Scanning transmission electron microscopy (STEM) images and electron energy loss spectroscopy (EELS) were acquired in an aberration-corrected FEI Titan transmission electron microscope operated at a primary electron energy of 300 keV. The microscope is equipped with a probe spherical-aberration corrector that allows for a ~0.1 nm spatial resolution, as well as a Wien-filter monochromator that provides an energy resolution of ~ 0.3 eV. EELS was acquired using a spectral dispersion of 0.2 eV per channel for the spectrometer. A convergence semi-angle of 13.7 mrad is used for both STEM imaging and EELS. For EELS, a collection semi-angle of 8.3 mrad is used. For HAADF STEM imaging, a 70 mrad collection inner angle is used. Elemental and at. % distribution maps were extracted from EELS spectrum images. Digital Micrograph (Gatan, Inc., USA) is utilized for data acquisition and processing. The X-ray powder diffraction (XRD) data was collected on a laboratory Bruker D8 Focus diffractometer (40 kV, 40 mA, sealed Cu X-ray tube, Kα1 1.540596 Å, Kα2 1.544493 Å) with a Ni filter and LynxEye position sensitive detector at room temperature. Gas product was analyzed on-line using a gas chromatography-mass spectrometer (GCMS-QP2010SE, Shimadzu). The liquid product was collected for each potential and

analyzed by a 300 MHz NMR spectrometer (Bruker), with Dimethyl sulfoxide (DMSO) as internal standards.

Synthesis of Cu_1@n-C_3N_4. In typical synthesis of Cu_1@n-C_3N_4, 10 g of urea and 268 mg of $CuCl_2 \cdot 2H_2O$ were dissolved in 20 mL of deionized water, the solution was stirred for 1 h and dried at 80 °C for 12 h to remove water. The dried mixture was calcined at 550 °C for 2 h with a ramping rate of 25 °C min^{-1} under a high purity argon (⩾99.999 %) atmosphere. After pyrolysis, a dark yellow power derived was used directly for characterization and catalysis test without acid leaching. The resulting powder was referred to as Cu_1@n-C_3N_4-27 %. Additional product was obtained with the amount of $CuCl_2 \cdot 2H_2O$ changed to 67 mg while the other conditions remain the same, and the obtained product was referred to as Cu_1@n-C_3N_4-10 %. Finally, a product synthesized without a copper salt while the other conditions remain the same was referred to as C_3N_4.

To synthesize Cu cluster-loaded C_3N_4, 50 mg of $CuCl_2 \cdot 2H_2O$ and 50 mg of C_3N_4 were added to 10 mL of deionized water, sonicated for 5 min, and stirred for 1 h to obtain a stock solution A. 22 mg of $NaBH_4$ was dissolved in 10 mL of deionized water to form a stock solution B. After that, the stock solution B was added dropwise to A, and the stirring was continued for 1 h, followed by centrifugation, washing with deionized water three times, and vacuum drying at 50 °C degrees for 12 h. The product was referred to as Cu clusters-C_3N_4.

Electrocatalytic studies. The catalyst ink was prepared from a mixture of catalyst (20 mg), deionized-H_2O (2ml), iso-propanol (2ml) and 0.15 ml Nafion solution. The mixture was sonicated for at least an hour to form a uniformed suspension. Working electrodes were prepared by drop-casting 0.4 ml of catalyst ink onto the GDL (~1cm^2) and wait till it's dry at ambient conditions. Electrochemical measurements were performed by using an Autolab 302 potentiostat (Metrohm). A Hg/HgO electrode (Koslow Scientific) was used as the reference electrode. IrO_2 powder deposited on GDLs was used as the counter electrode. Alkaline electrolytes (1 mol/L KOH) were flown through both the cathodic and anodic compartments of the GDE

cell at 0.5 ml/min by using a syringe pump. CO gas is introduced into the gas chamber at a constant rate of 20 sccm. The gas-phase products were analyzed online using gas chromatograph-mass spectrometry (GC-MS-QP2010SE Shimadzu) and liquid-phase products were analyzed after ~12 min of reaction at each potential using nuclear magnetic resonance (NMR) spectroscopy. All potentials discussed in this work were converted to the RHE scale by following the equation E (vs. RHE) = E (vs. Hg/HgO) + 0.14 V + 0.0591 V × pH. The electrochemical test was done with iR correction. A scheme showing the electrochemical set-up was included in **Figure S21**.

CO stripping voltammetry was measured with a rotating disk electrode. For a typical experiment, a catalyst ink, consisting of 1 mg of catalyst, 0.9 ml DI-H_2O, 0.1 ml iso-propanol and 5µl Nafion solution, was prepared. A drop of 20 µl catalyst ink was pipetted onto the glassy carbon electrode and wait until it's dry. Before the cyclic voltammetry test, the electrode was held at 0.05 V (vs. RHE), while pure CO gas was purged into the electrolyte (0.1 mol/L KOH) for 10 min. Then the electrolyte was purged with Ar gas for 40 min to remove the CO dissolved in the electrolyte. Cyclic voltammograms (CVs) were recorded between 0.05 V and 1.05 V (vs. RHE) at 50 mV/s.

CO Diffuse reflectance infrared Fourier transform spectroscopy (FTIR). FTIR spectra for CO adsorption were recorded on a Nicolet 6700 spectrometer equipped with a mercury cadmium telluride (MCT) detector cooled by liquid N_2. Before CO adsorption, samples were evacuated at 200 °C for 2 h, and then cooled to 25 °C for CO adsorption. The DRIFTS spectra were collected at 25 °C, after a 30-min purging with Ar. The spectra were collected with a resolution of 4 cm^{-1} and accumulation of 100 scans for each sample.

X-ray absorption spectroscopy. In situ X-ray absorption spectroscopy (XAS) experiments were performed at the 10-BM beamline at the Advanced Photon Source (APS) at Argonne National Laboratory. All measurements were performed at the Cu K edge (8.979 keV) in transmission mode in fast scan from 250 eV below the edge to 550 eV above the edge, which took approximately 10 minutes per scan. The XANES energies were calibrated using Cu foil and set to be 8.8932 eV (**Table S2**). Samples were pressed

into a stainless-steel sample holder and placed in a sample cell. The cell was sealed and transferred to the beamline for measurement. At the Cu K edge, the Cu-N (CN=1, R=2.1 Å) scattering pair was simulated. S_o^2 was calibrated by fitting the foil. This value was found to be 0.85. A least squared fit the first shell of r-space and isolated q- space were performed on the k^2 weighted Fourier transform data over the range 2.7 to 10 $Å^{-1}$ in each spectrum to fit the magnitude and imaginary components. The pre-edge feature at 8.978 eV (**Figure 1e**) is a result of s-p hybridization in transition metals and can be attributed to the s → d electron transition of Cu^{2+}.

In-situ X-ray absorption spectroscopy. A lab-made acryl kit was used for the in-situ X-ray measurements.(*63*) In-situ XAS measurements of Cu K-edge were conducted with the fluorescence mode, in the 7-BM beamline at National Synchrotron Light Source II (NSLS-II) at Brookhaven National Laboratory. Prior to the in-situ XAS study, the pristine Cu_1@n-C_3N_4-27% was measured as a reference. 1M KOH was used as electrolyte and 5% CO (95% Ar) as gas reactant. Four cathodic potentials were investigated, 0 V, −0.5 V, −0.75 V and −1 V (vs. RHE). The spectrum of Cu foil was recorded to calibrate the edge energy (E_0) of the samples under the same experiment conditions. For each sample, 50 scans (30-34 seconds each) were averaged together. The sample was under reaction conditions for 25 – 30 minutes, and all 50 scans were identical.

X-ray photoelectron spectroscopy (XPS). XPS measurements were analyzed using a Kratos Analytical AXIS Ultra DLD spectrometer. The analyzing chamber of the spectrometer typically maintained an ultra-high vacuum (UHV) working pressure below 3.6×10^{-7} Pa. Spectra were collected using a monochromatic Al Kα X-ray source with 20 eV analyzer pass energy and a 0.7 mm × 0.3 mm spot size. Spectra were evaluated using Casa XPS software.

Computational Methods

The first-principles density functional theory (DFT)(*64, 65*) calculations with plane wave basis set were

performed using the Vienna ab initio simulation package (VASP) software(*66, 67*). The projector augmented wave (PAW)(*68, 69*) pseudopotential was used to describe the core electrons. The cut-off energies of plane wave basis set were set as 400 eV, 400 eV, and 500 eV to expand the wave functions for CuPc molecule, CuN_2 site and metallic Cu surface, respectively. The generalized gradient approximation (GGA) of the revised Perdew, Burke and Ernzernhof (RPBE)(*70*) functionals were used to describe the electronic exchange and correlation energy term. The aqueous environment of the electrolyte was treated with a continuum dielectric model as implemented by the Hennig group in the VASPsol code(*71*). The relative permittivity was set as 78.4 to model the water environment. CuN_2 moieties embedded in a carbon nitride (C_3N_4) layer, p(2×2) Cu(100), and p(2×2) Cu(111) were modeled as the active sites to catalyze CO reduction reaction. The bond length of Cu-Cu in bulk Cu was predicted to be 2.60 Å. A rhombic C_3N_4 layered structure was modeled using 14 atoms, including 6 carbon atoms and 8 nitrogen atoms, and with a lattice parameter of $a = b = 7.19$ Å. In addition, a 20 Å vacuum region was added perpendicularly to the C_3N_4 layer to separate periodic images. The Brillouin zone was sampled by Monkhorst(*72*) 5×5×1, 5×5×1, 5×5×1, 1×1×1 k-point grid for models of CuN_2 active site, p(2×2) Cu(100), p(2×2) Cu(111), and Cu-Pc molecule, respectively. Bader charge analysis(*73*) was used to calculate the total valence electron number of Cu in Cu-N_2 and Cu-Pc.

In structural optimization calculations, the atom positions were relaxed until the force on each ion fell below 0.01e V/Å. In our molecular vibration frequency calculation of Cu-N_2 site, all the C and N atoms were fixed, whereas the Cu and H atoms were allowed to make vibrational motion. As for the vibrational frequency calculation of molecule in gas phase, all the atoms allow to make vibrational motion. The computational hydrogen electrode (CHE) was used to calculate the free energy of corresponding reaction intermediates and evaluate the limiting potential of CORR on various active sites. All computations were conducted under electrode potential U=0 V. The free energy of a chemical reaction was calculated as follows

$$\Delta G = \Delta E_{DFT} + \Delta E_{ZPE} + \Delta H_T - T\Delta S$$

where ΔE_{ZPE} is the energy change derived from DFT calculation, ΔE_{ZPE} is the zero-point energy change, ΔH_T is the enthalpy change from 0 K to T K, and ΔS is entropy change for the reaction. ZPE corrections were calculated as ZPE $=\sum \frac{1}{2} h\nu_i$, where h is the Planck's constant and ν_i is the frequency of the corresponding vibrational mode of binding molecules. The vibrational heat capacity integration $\int_0^T C_p(t)dt$ was used to calculate the ΔH_T. The entropy term is calculated as $S = k_B * \sum_i (\frac{h\nu_i}{k_B T} * \frac{1}{\exp\left(\frac{h\nu_i}{k_B T}\right)-1} - \ln\left[1-\exp\left(-\frac{h\nu_i}{k_B T}\right)\right])$. Where, T is the temperature of reaction, S is the vibrational entropy, h is the Planck's constant, k_B is the Boltzmann constant, vi is the frequency of the ith vibrational mode.

For the molecules, the free energies were calculated as follow:

$$G = E_{DFT} + E_{ZPE} + H_T - TS + \frac{n}{2} k_B T$$

where n is eight for nonlinear molecule and seven for linear molecule. We adopted the implicit solvation model to predict the free energy of CH_3COO^- and C_2H_5OH in aqueous solution. The free energy correction for molecule in aqueous solution was predicted to be -0.18 eV for C_2H_5OH, and -0.32 eV for CH_3COO^-, respectively.

Validation of CO adsorption on Cu(111)/Cu(100) surface using RPBE functional

In experiment, the measured CO coverage on Cu(100) or Cu(111) surface was reported to be higher than 0.25(*74*). To validate our DFT method using the experimental result, we constructed a p(2×2) Cu(100) and Cu(111) surfaces with a CO molecule (coverage of 0.25) adsorbed on and predicted the corresponding CO adsorption energies to be -0.53 eV on Cu(100) surface and -0.47 eV on Cu(111) (Table S7). These predictions agrees well with experimentally measured CO adsorption energies of -0.53 eV on Cu(100) surface and -0.49 eV on Cu(111).(*74*) This result suggests that RPBE shows accurate prediction for CO adsorption on Cu surface, in line with the conclusion of previous work.(*75*)

Calculations for energy barrier/activation energy

Moreover, the constrained ab initio molecular dynamics (AIMD) calculation(*76*) with reaction coordination gradually changing from the initial to the final state (slow growth method) was applied to predict the activation energy for the C-C coupling reaction via the E-R mechanism at 300K. The simulation was conducted using the canonical ensemble without considering the interaction between CO molecules. Nose-Hoover thermostat was used to keep temperature constant at 300 K(*77*). Time step in AIMD was set to be 1 femtosecond. As shown in Figure S31a, we predicted the activation energy for C-C coupling via E-R mechanism to be 0.80 eV.

In addition, the nudged elastic band (NEB) calculations(*78*) were performed to identify the transition state and predict the activation energy for the C-C coupling reaction via the L-H mechanism and CO hydrogenation reaction. In NEB calculation, the force along and perpendicular to the reaction path were relaxed to less than 0.05 eV/ Å. The activation energy for C-C coupling via L-H mechanism was predicted to be 2.45 eV (Figure S31b). In addition, the activation energies for CO hydrogenation were predicted to be 0.55 eV using proton as the hydrogen source and 0.83 eV using water as the hydrogen source, respectively (Figure S35 and Supplementary Note 2).

Calculations for methane pathway

The bifurcation step between methane pathway and C2 product pathway on Cu-C_3N_4 site is as follows (Figure S32). Following the methane pathway, the adsorbed CHO will be protonated to form *CHOH, whereas the adsorbed CHO will be coupled with other CO to form *CO-CHO through C2 product pathway. We predicted the free energy change for *CHO -> *CHOH step to be 0.55 eV, higher than that of 0.22 eV for CHO-CO coupling step. This result indicates that CHO-CO coupling reaction is more thermodynamically favorable than CHO protonation, explaining the high C2 product selectivity on Cu-C_3N_4 site. Moreover, we predicted the free energy change to be -0.15 eV for *CH-CO -> *CH_2CO step and 0.94 eV for *CH-CO -> *CHCOH step. This result further reveals that acetate pathway is more favorable than ethylene or ethanol pathway.

References

1. D. T. Whipple, P. J. A. Kenis, Prospects of CO_2 Utilization via Direct Heterogeneous Electrochemical Reduction. *J. Phys. Chem. Lett.* **1**, 3451-3458 (2010).
2. P. De Luna, C. Hahn, D. Higgins, S. A. Jaffer, T. F. Jaramillo, E. H. Sargent, What would it take for renewably powered electrosynthesis to displace petrochemical processes? *Science* **364**, eaav3506 (2019).
3. H. Xiao, T. Cheng, W. A. Goddard, R. Sundararaman, Mechanistic Explanation of the pH Dependence and Onset Potentials for Hydrocarbon Products from Electrochemical Reduction of CO on Cu (111). *J. Am. Chem. Soc.* **138**, 483-486 (2016).
4. C. T. Dinh, T. Burdyny, M. G. Kibria, A. Seifitokaldani, C. M. Gabardo, F. P. G. de Arquer, A. Kiani, J. P. Edwards, P. De Luna, O. S. Bushuyev, C. Q. Zou, R. Quintero-Bermudez, Y. J. Pang, D. Sinton, E. H. Sargent, CO_2 electroreduction to ethylene via hydroxide-mediated copper catalysis at an abrupt interface. *Science* **360**, 783-787 (2018).
5. J. A. Rabinowitz, M. W. Kanan, The future of low-temperature carbon dioxide electrolysis depends on solving one basic problem. *Nat. Commun.* **11**, 5231 (2020).
6. Y. Hori, H. Wakebe, T. Tsukamoto, O. Koga, Electrocatalytic process of CO selectivity in electrochemical reduction of CO_2 at metal electrodes in aqueous media. *Electrochim. Acta* **39**, 1833-1839 (1994).
7. B. A. Rosen, A. Salehi-Khojin, M. R. Thorson, W. Zhu, D. T. Whipple, P. J. A. Kenis, R. I. Masel, Ionic Liquid–Mediated Selective Conversion of CO_2 to CO at Low Overpotentials. *Science* **334**, 643 (2011).

8. K. J. P. Schouten, Z. Qin, E. Pérez Gallent, M. T. M. Koper, Two Pathways for the Formation of Ethylene in CO Reduction on Single-Crystal Copper Electrodes. *J. Am. Chem. Soc.* **134**, 9864-9867 (2012).

9. S. Ma, M. Sadakiyo, M. Heima, R. Luo, R. T. Haasch, J. I. Gold, M. Yamauchi, P. J. A. Kenis, Electroreduction of Carbon Dioxide to Hydrocarbons Using Bimetallic Cu–Pd Catalysts with Different Mixing Patterns. *J. Am. Chem. Soc.* **139**, 47-50 (2017).

10. M. Jouny, W. Luc, F. Jiao, High-rate electroreduction of carbon monoxide to multi-carbon products. *Nat. Catal.*, (2018).

11. D. Raciti, C. Wang, Electrochemical alternative to Fischer–Tropsch. *Nat. Catal.* **1**, 741-742 (2018).

12. J. Li, Z. Wang, C. McCallum, Y. Xu, F. Li, Y. Wang, C. M. Gabardo, C.-T. Dinh, T.-T. Zhuang, L. Wang, J. Y. Howe, Y. Ren, E. H. Sargent, D. Sinton, Constraining CO coverage on copper promotes high-efficiency ethylene electroproduction. *Nat. Catal.* **2**, 1124-1131 (2019).

13. H. Mistry, R. Reske, Z. Zeng, Z.-J. Zhao, J. Greeley, P. Strasser, B. R. Cuenya, Exceptional Size-Dependent Activity Enhancement in the Electroreduction of CO_2 over Au Nanoparticles. *J. Am. Chem. Soc.* **136**, 16473-16476 (2014).

14. C. G. Morales-Guio, E. R. Cave, S. A. Nitopi, J. T. Feaster, L. Wang, K. P. Kuhl, A. Jackson, N. C. Johnson, D. N. Abram, T. Hatsukade, C. Hahn, T. F. Jaramillo, Improved CO_2 reduction activity towards C_{2+} alcohols on a tandem gold on copper electrocatalyst. *Nat. Catal.* **1**, 764-771 (2018).

15. S. Mezzavilla, S. Horch, I. E. L. Stephens, B. Seger, I. Chorkendorff, Structure Sensitivity in the Electrocatalytic Reduction of CO_2 with Gold Catalysts. *Angew. Chem. Int. Ed.* **58**, 3774-3778 (2019).

16. Q. Lu, J. Rosen, Y. Zhou, G. S. Hutchings, Y. C. Kimmel, J. G. Chen, F. Jiao, A selective and efficient electrocatalyst for carbon dioxide reduction. *Nat. Commun.* **5**, 3242 (2014).

17. T. Zheng, K. Jiang, N. Ta, Y. Hu, J. Zeng, J. Liu, H. Wang, Large-Scale and Highly Selective CO_2 Electrocatalytic Reduction on Nickel Single-Atom Catalyst. *Joule* **3**, 14 (2018).

18. Y. Wang, H. Su, Y. He, L. Li, S. Zhu, H. Shen, P. Xie, X. Fu, G. Zhou, C. Feng, D. Zhao, F. Xiao, X. Zhu, Y. Zeng, M. Shao, S. Chen, G. Wu, J. Zeng, C. Wang, Advanced Electrocatalysts with Single-Metal-Atom Active Sites. *Chem. Rev.* **120**, 12217–12314 (2020).

19. F. Calle-Vallejo, M. T. M. Koper, Theoretical Considerations on the Electroreduction of CO to C_2 Species on Cu(100) Electrodes. *Angew. Chem. Int. Ed.* **52**, 7282-7285 (2013).

20. J. H. Montoya, C. Shi, K. Chan, J. K. Nørskov, Theoretical Insights into a CO Dimerization Mechanism in CO_2 Electroreduction. *J. Phys. Chem. Lett.* **6**, 2032-2037 (2015).

21. T. Cheng, H. Xiao, W. A. Goddard, Full atomistic reaction mechanism with kinetics for CO reduction on Cu(100) from ab initio molecular dynamics free-energy calculations at 298 K. *Proc. Nat. Acad. Sci.* **114**, 1795 (2017).

22. A. J. Garza, A. T. Bell, M. Head-Gordon, Mechanism of CO_2 Reduction at Copper Surfaces: Pathways to C_2 Products. *ACS Catal.* **8**, 1490-1499 (2018).

23. Y. Pang, J. Li, Z. Wang, C.-S. Tan, P.-L. Hsieh, T.-T. Zhuang, Z.-Q. Liang, C. Zou, X. Wang, P. De Luna, J. P. Edwards, Y. Xu, F. Li, C.-T. Dinh, M. Zhong, Y. Lou, D. Wu, L.-J. Chen, E. H. Sargent, D. Sinton, Efficient electrocatalytic conversion of carbon monoxide to propanol using fragmented copper. *Nat. Catal.* **2**, 251-258 (2019).

24. M. Jouny, G. S. Hutchings, F. Jiao, Carbon monoxide electroreduction as an emerging platform for carbon utilization. *Nat. Catal.* **2**, 1062-1070 (2019).

25. D. Raciti, C. Wang, Recent Advances in CO_2 Reduction Electrocatalysis on Copper. *ACS Energy Letters* **3**, 1545-1556 (2018).

26. S. Nitopi, E. Bertheussen, S. B. Scott, X. Liu, A. K. Engstfeld, S. Horch, B. Seger, I. E. L. Stephens, K. Chan, C. Hahn, J. K. Nørskov, T. F. Jaramillo, I. Chorkendorff, Progress and Perspectives of Electrochemical CO_2 Reduction on Copper in Aqueous Electrolyte. *Chem. Rev.* **119**, 7610-7672 (2019).

27. A. Loiudice, P. Lobaccaro, E. A. Kamali, T. Thao, B. H. Huang, J. W. Ager, R. Buonsanti, Tailoring Copper Nanocrystals towards C_2 Products in Electrochemical CO_2 Reduction. *Angew. Chem. Int. Ed.* **55**, 5789-5792 (2016).

28. E. Pérez-Gallent, M. C. Figueiredo, F. Calle-Vallejo, M. T. M. Koper, Spectroscopic Observation of a Hydrogenated CO Dimer Intermediate During CO Reduction on Cu(100) Electrodes. *Angew. Chem. Int. Ed.* **56**, 3621-3624 (2017).

29. J. D. Goodpaster, A. T. Bell, M. Head-Gordon, Identification of Possible Pathways for C–C Bond Formation during Electrochemical Reduction of CO_2: New Theoretical Insights from an Improved Electrochemical Model. *J. Phys. Chem. Lett.* **7**, 1471-1477 (2016).

30. T. Cheng, H. Xiao, W. A. Goddard, Free-Energy Barriers and Reaction Mechanisms for the Electrochemical Reduction of CO on the Cu(100) Surface, Including Multiple Layers of Explicit Solvent at pH 0. *J. Phys. Chem. Lett.* **6**, 4767-4773 (2015).

31. D. Raciti, L. Cao, K. J. T. Livi, P. F. Rottmann, X. Tang, C. Li, Z. Hicks, K. H. Bowen, K. J. Hemker, T. Mueller, C. Wang, Low-Overpotential Electroreduction of Carbon Monoxide Using Copper Nanowires. *ACS Catal.* **7**, 4467-4472 (2017).

32. K. J. P. Schouten, E. Pérez Gallent, M. T. M. Koper, The influence of pH on the reduction of CO and CO_2 to hydrocarbons on copper electrodes. *J. Electroanal. Chem.* **716**, 53-57 (2014).

33. D. Raciti, M. Mao, J. H. Park, C. Wang, Local pH Effect in the CO_2 Reduction Reaction on High-Surface-Area Copper Electrocatalysts. *J. Electrochem. Soc.* **165**, F799-F804 (2018).

34. W. Luc, X. Fu, J. Shi, J.-J. Lv, M. Jouny, B. Hee Ko, Y. Xu, Q. Tu, X. Hu, J. Wu, Q. Yue, Y. Liu, F. Jiao, Y. Kang, Two-dimensional copper nanosheets for electrochemical reduction of carbon monoxide to acetate. *Nat. Catal.* **2**, 423-430 (2019).

35. X. Liu, P. Schlexer, J. Xiao, Y. Ji, L. Wang, R. B. Sandberg, M. Tang, K. S. Brown, H. Peng, S. Ringe, C. Hahn, T. F. Jaramillo, J. K. Nørskov, K. Chan, pH effects on the electrochemical reduction of $CO(_2)$ towards C_2 products on stepped copper. *Nat. Commun.* **10**, 32 (2019).

36. A. A. Peterson, J. K. Nørskov, Activity Descriptors for CO_2 Electroreduction to Methane on Transition-Metal Catalysts. *J. Phys. Chem. Lett.* **3**, 251-258 (2012).

37. J. Liu, T. Zhang, Z. Wang, G. Dawson, W. Chen, Simple pyrolysis of urea into graphitic carbon nitride with recyclable adsorption and photocatalytic activity. *J. Mater. Chem.* **21**, 14398-14401 (2011).

38. L. Zhang, R. Long, Y. Zhang, D. Duan, Y. Xiong, Y. Zhang, Y. Bi, Direct Observation of Dynamic Bond Evolution in Single-Atom Pt/C_3N_4 Catalysts. *Angew. Chem. Int. Ed.* **59**, 6224-6229 (2020).

39. C. G. Schroer, M. Kuhlmann, T. F. Günzler, B. Lengeler, M. Richwin, B. Griesebock, D. Lützenkirchen-Hecht, R. Frahm, E. Ziegler, A. Mashayekhi, D. R. Haeffner, J. D. Grunwaldt, A. Baiker, Mapping the chemical states of an element inside a sample using tomographic x-ray absorption spectroscopy. *Appl. Phys. Lett.* **82**, 3360-3362 (2003).

40. J. Jiao, R. Lin, S. Liu, W.-C. Cheong, C. Zhang, Z. Chen, Y. Pan, J. Tang, K. Wu, S.-F. Hung, H. M. Chen, L. Zheng, Q. Lu, X. Yang, B. Xu, H. Xiao, J. Li, D. Wang, Q. Peng, C. Chen, Y. Li, Copper atom-pair catalyst anchored on alloy nanowires for selective and efficient electrochemical reduction of CO_2. *Nat. Chem.* **11**, 222-228 (2019).

41. L. S. Kau, D. J. Spira-Solomon, J. E. Penner-Hahn, K. O. Hodgson, E. I. Solomon, X-ray absorption edge determination of the oxidation state and coordination number of copper. Application to the type 3 site in Rhus vernicifera laccase and its reaction with oxygen. *J. Am. Chem. Soc.* **109**, 6433-6442 (1987).

42. D. T. Whipple, E. C. Finke, P. J. A. Kenis, Microfluidic Reactor for the Electrochemical Reduction of Carbon Dioxide: The Effect of pH. *Electrochem. Solid-State Lett.* **13**, B109 (2010).

43. Y. Wang, H. Shen, K. J. T. Livi, D. Raciti, H. Zong, J. Gregg, M. Onadeko, Y. Wan, A. Watson, C. Wang, Copper Nanocubes for CO_2 Reduction in Gas Diffusion Electrodes. *Nano Lett.* **19**, 8461-8468 (2019).

44. B. Qiao, A. Wang, X. Yang, L. F. Allard, Z. Jiang, Y. Cui, J. Liu, J. Li, T. Zhang, Single-atom catalysis of CO oxidation using Pt_1/FeO_x. *Nat. Chem.* **3**, 634-641 (2011).

45. P. Xie, T. Pu, A. Nie, S. Hwang, S. C. Purdy, W. Yu, D. Su, J. T. Miller, C. Wang, Nanoceria-Supported Single-Atom Platinum Catalysts for Direct Methane Conversion. *ACS Catal.* **8**, 4044-4048 (2018).

46. A. Verdaguer-Casadevall, C. W. Li, T. P. Johansson, S. B. Scott, J. T. McKeown, M. Kumar, I. E. L. Stephens, M. W. Kanan, I. Chorkendorff, Probing the Active Surface Sites for CO Reduction on Oxide-Derived Copper Electrocatalysts. *J. Am. Chem. Soc.* **137**, 9808-9811 (2015).

47. Y. Lei, H. Zhao, R. D. Rivas, S. Lee, B. Liu, J. Lu, E. Stach, R. E. Winans, K. W. Chapman, J. P. Greeley, J. T. Miller, P. J. Chupas, J. W. Elam, Adsorbate-Induced Structural Changes in 1–3 nm Platinum Nanoparticles. *J. Am. Chem. Soc.* **136**, 9320-9326 (2014).

48. D. Friebel, V. Viswanathan, D. J. Miller, T. Anniyev, H. Ogasawara, A. H. Larsen, C. P. O'Grady, J. K. Nørskov, A. Nilsson, Balance of Nanostructure and Bimetallic Interactions in Pt Model Fuel Cell Catalysts: In Situ XAS and DFT Study. *J. Am. Chem. Soc.* **134**, 9664-9671 (2012).

49. J. Li, K. Chang, H. Zhang, M. He, W. A. Goddard, J. G. Chen, M.-J. Cheng, Q. Lu, Effectively Increased Efficiency for Electroreduction of Carbon Monoxide Using

Supported Polycrystalline Copper Powder Electrocatalysts. *ACS Catal.* **9**, 4709-4718 (2019).

50. S. Fletcher, Tafel slopes from first principles. *J. Solid State Electrochem.* **13**, 537-549 (2009).

51. X. Wang, J. F. de Araújo, W. Ju, A. Bagger, H. Schmies, S. Kühl, J. Rossmeisl, P. Strasser, Mechanistic reaction pathways of enhanced ethylene yields during electroreduction of CO_2–CO co-feeds on Cu and Cu-tandem electrocatalysts. *Nat. Nanotech.* **14**, 1063-1070 (2019).

52. T. Cheng, H. Xiao, W. A. Goddard, Nature of the Active Sites for CO Reduction on Copper Nanoparticles; Suggestions for Optimizing Performance. *J. Am. Chem. Soc.* **139**, 11642-11645 (2017).

53. H. Bao, Y. Qiu, X. Peng, J.-a. Wang, Y. Mi, S. Zhao, X. Liu, Y. Liu, R. Cao, L. Zhuo, J. Ren, J. Sun, J. Luo, X. Sun, Isolated copper single sites for high-performance electroreduction of carbon monoxide to multicarbon products. *Nat. Commun.* **12**, 238 (2021).

54. A. Guan, Z. Chen, Y. Quan, C. Peng, Z. Wang, T.-K. Sham, C. Yang, Y. Ji, L. Qian, X. Xu, G. Zheng, Boosting CO_2 Electroreduction to CH_4 via Tuning Neighboring Single-Copper Sites. *ACS Energy Letters* **5**, 1044-1053 (2020).

55. L. Ji, L. Li, X. Ji, Y. Zhang, S. Mou, T. Wu, Q. Liu, B. Li, X. Zhu, Y. Luo, X. Shi, A. M. Asiri, X. Sun, Highly Selective Electrochemical Reduction of CO_2 to Alcohols on an FeP Nanoarray. *Angew. Chem. Int. Ed.* **59**, 758-762 (2020).

56. P.-P. Yang, X.-L. Zhang, F.-Y. Gao, Y.-R. Zheng, Z.-Z. Niu, X. Yu, R. Liu, Z.-Z. Wu, S. Qin, L.-P. Chi, Y. Duan, T. Ma, X.-S. Zheng, J.-F. Zhu, H.-J. Wang, M.-R. Gao, S.-H.

Yu, Protecting Copper Oxidation State via Intermediate Confinement for Selective CO_2 Electroreduction to C_{2+} Fuels. *J. Am. Chem. Soc.* **142**, 6400-6408 (2020).

57. F. Pan, H. Zhang, K. Liu, D. Cullen, K. More, M. Wang, Z. Feng, G. Wang, G. Wu, Y. Li, Unveiling Active Sites of CO_2 Reduction on Nitrogen-Coordinated and Atomically Dispersed Iron and Cobalt Catalysts. *ACS Catal.* **8**, 3116-3122 (2018).

58. W. Ju, A. Bagger, G.-P. Hao, A. S. Varela, I. Sinev, V. Bon, B. Roldan Cuenya, S. Kaskel, J. Rossmeisl, P. Strasser, Understanding activity and selectivity of metal-nitrogen-doped carbon catalysts for electrochemical reduction of CO_2. *Nat. Commun.* **8**, 944 (2017).

59. D. Karapinar, N. T. Huan, N. Ranjbar Sahraie, J. Li, D. Wakerley, N. Touati, S. Zanna, D. Taverna, L. H. Galvão Tizei, A. Zitolo, F. Jaouen, V. Mougel, M. Fontecave, Electroreduction of CO_2 on Single-Site Copper-Nitrogen-Doped Carbon Material: Selective Formation of Ethanol and Reversible Restructuration of the Metal Sites. *Angew. Chem. Int. Ed.* **58**, 15098-15103 (2019).

60. Z. Weng, Y. Wu, M. Wang, J. Jiang, K. Yang, S. Huo, X.-F. Wang, Q. Ma, G. W. Brudvig, V. S. Batista, Active sites of copper-complex catalytic materials for electrochemical carbon dioxide reduction. *Nat. Commun.* **9**, 1-9 (2018).

61. H. Li, Y. Li, M. T. M. Koper, F. Calle-Vallejo, Bond-Making and Breaking between Carbon, Nitrogen, and Oxygen in Electrocatalysis. *J. Am. Chem. Soc.* **136**, 15694-15701 (2014).

62. Y. Jiao, Y. Zheng, P. Chen, M. Jaroniec, S.-Z. Qiao, Molecular Scaffolding Strategy with Synergistic Active Centers To Facilitate Electrocatalytic CO_2 Reduction to Hydrocarbon/Alcohol. *J. Am. Chem. Soc.* **139**, 18093-18100 (2017).

63. J. H. Lee, S. Kattel, Z. Jiang, Z. Xie, S. Yao, B. M. Tackett, W. Xu, N. S. Marinkovic, J. G. Chen, Tuning the activity and selectivity of electroreduction of CO2 to synthesis gas using bimetallic catalysts. *Nat. Commun.* **10**, 3724 (2019).

64. P. Hohenberg, W. Kohn, Inhomogeneous Electron Gas. *Phys. Rev.* **136**, B864-B871 (1964).

65. W. Kohn, L. J. Sham, Self-Consistent Equations Including Exchange and Correlation Effects. *Phys. Rev.* **140**, A1133-A1138 (1965).

66. G. Kresse, J. Hafner, Ab initio molecular dynamics for liquid metals. *Phys. Rev. B* **47**, 558-561 (1993).

67. G. Kresse, J. Furthmüller, Efficiency of ab-initio total energy calculations for metals and semiconductors using a plane-wave basis set. *Comput. Mater. Sci.* **6**, 15-50 (1996).

68. P. E. Blöchl, Projector augmented-wave method. *Phys. Rev. B* **50**, 17953-17979 (1994).

69. G. Kresse, D. Joubert, From ultrasoft pseudopotentials to the projector augmented-wave method. *Phys. Rev. B* **59**, 1758-1775 (1999).

70. B. Hammer, L. B. Hansen, J. K. Nørskov, Improved adsorption energetics within density-functional theory using revised Perdew-Burke-Ernzerhof functionals. *Phys. Rev. B* **59**, 7413-7421 (1999).

71. K. Mathew, R. Sundararaman, K. Letchworth-Weaver, T. Arias, R. G. Hennig, Implicit solvation model for density-functional study of nanocrystal surfaces and reaction pathways. *J. Chem. Phys.* **140**, 084106 (2014).

72. H. J. Monkhorst, J. D. Pack, Special points for Brillouin-zone integrations. *Phys. Rev. B* **13**, 5188-5192 (1976).

73. E. Sanville, S. D. Kenny, R. Smith, G. Henkelman, Improved grid-based algorithm for Bader charge allocation. *J. Comput. Chem.* **28**, 899-908 (2007).

74. S. Vollmer, G. Witte, C. Wöll, Determination of site specific adsorption energies of CO on copper. *Catal. Lett.* **77**, 97-101 (2001).

75. C. N. Lininger, J. A. Gauthier, W.-L. Li, E. Rossomme, V. V. Welborn, Z. Lin, T. Head-Gordon, M. Head-Gordon, A. T. Bell, Challenges for density functional theory: calculation of CO adsorption on electrocatalytically relevant metals. *Phys. Chem. Chem. Phys.* **23**, 9394-9406 (2021).

76. H. Oberhofer, C. Dellago, P. L. Geissler, Biased sampling of nonequilibrium trajectories: Can fast switching simulations outperform conventional free energy calculation methods? *J. Phys. Chem. B* **109**, 6902-6915 (2005).

77. W. G. Hoover, Canonical dynamics: Equilibrium phase-space distributions. *Phys. Rev. A* **31**, 1695 (1985).

78. G. Henkelman, B. P. Uberuaga, H. Jónsson, A climbing image nudged elastic band method for finding saddle points and minimum energy paths. *J. Chem. Phys.* **113**, 9901-9904 (2000).

Acknowledgement

Funding Support: This work is supported by National Science Foundation (CBET- 1930013 and CBET-1803482) and Department of Energy (DE-EE0008501). This research used resources of the Center for Functional Nanomaterials (CFN) and the National Synchrotron Light Source II, both are U.S. Department of Energy (DOE) Office of Science user facilities operated for the DOE Office of Science by Brookhaven National Laboratory under Contract No. DE-SC0012704. Beamline operations were supported in part by the Synchrotron Catalysis Consortium, (U.S. DOE, Office of Basic Energy Sciences, Grant No. DE-SC0012335).

Author Contribution: Y.W. and Chao.W. conceived the concept drafted the original version of the manuscript. Y.W., B.X., H.S., Canhui.W., D.R., H.Z., W.X., Z.L., G.Z., J.V. performed the synthesis, characterization and electrocatalytic studies. N. L., Z.X., N.M., J.G.C. and J.M. conducted the XAS studies. B. L. and G.W. developed the computational methods and conducted the simulations. All authors approved the final version of manuscript.

Data and Materials Availability: All data needed to evaluate the conclusions in the paper are present in the paper and/or the Supplementary Materials.

Competing Interests: All authors declare that they have no competing interests.